Open Ceramics 7 (2021) 100162

Contents lists available at ScienceDirect

Open Ceramics

journal homepage: www.sciencedirect.com/journal/open-ceramics

Large scale additive manufacturing of artificial stone components using binder jetting and their X-ray microtomography investigations

F. Gobbin [a,b], Hamada Elsayed [a,c,*], A. Italiano [b], J. Adrien [d], P. Colombo [a,e], E. Maire [d]

[a] University of Padova, Industrial Engineering Department, Padova, Italy
[b] Desamanera Srl, Rovigo, Italy
[c] Refractories, Ceramics and Building Materials Department, National Research Centre, El-Bohous Str., 12622, Cairo, Egypt
[d] Université de Lyon, INSA de Lyon, MATEIS CNRS UMR5510, 20 Avenue Albert Einstein, F, 69621, Villeurbanne Cedex, France
[e] Department of Materials Science and Engineering, Pennsylvania State University, University Park, PA, 16801, USA

ARTICLE INFO

Keywords:
Additive manufacturing
Binder jetting
Artificial stone
X-ray microtomography

ABSTRACT

Additive manufacturing of large scale parts is an innovative, challenging research field, with the potential of producing parts with complex structures, specific functional and structural properties. In this study, binder jetting was employed using two different large scale printers to fabricate non-structural parts made of artificial stone. The printing bed was comprised of aggregates (River sand and Poraver expanded glass) and reactive magnesium oxide and potassium phosphate powders, which were activated by selectively depositing water, layer after layer. The exothermic reaction between reactive powders and water generates *in situ* a hydraulic inorganic binder, that binds the aggregates in the bed. The reaction parameters were controlled to achieve a fast setting, enabling rapid printing at the macro-scale (in the range of tens of centimeters or meters). The influence of the voxel size of the printers on the microstructure and printing quality of the fabricated parts, their physical and mechanical properties as well as the *in situ* formation of the cement phase were investigated by X-ray microtomography.

1. Introduction

Additive Manufacturing (AM) is one of the most interesting technologies for the production of components of complex and customized shapes in low volumes, and becomes an integral part of processing, in the modern production organization, completing the transformation from rapid prototyping to rapid manufacturing and production of final objects [1,2]. Additive Manufacturing offers great advances in terms of customization, design freedom, flexibility and scalability, reduction of waste and on demand production [3,4]. Starting from the development of the stereolithography apparatus by C.W. Hull in the 1980s [5], several different additive manufacturing technologies (such as binder jetting (BJ), direct ink writing (DIW), fused deposition modeling (FDM), selective laser sintering (SLS), digital light processing (DLP), etc.) have been developed and applied to different classes of materials, including ceramics [6]. AM has been used, in the ceramic field, to fabricate parts for different applications, such as high temperature, piezoelectric, dental and energy storage components, bone scaffolds, filters, supports for catalysis, electrodes and complex lightweight engineered structures [7–14].

In recent years, research in the field of additive manufacturing has expanded into large scale fabrication using cement-based materials [15,16]. Although the interaction between the requirements for large-scale dimensions, in the range of tens of centimeters or meters, and fast production, providing also specific final properties to the components, is not straightforward, AM has been successfully employed for non-structural, art and design applications. There are also numerous studies aiming at making AM technologies suitable for the fabrication of parts capable to be employed in structural applications in the construction industry sector [17,18].

The main AM techniques used for the fabrication of structures at the macro-scale are based on extrusion (i.e. the flow of an inorganic paste through a nozzle) or a powder bed (i.e. the consolidation of a bed of particles via binder deposition). The extrusion-based deposition technology has the advance of enabling fast production, with the drawback of having limitations in the fabrication of complex shapes and overhangs, the optimization of the rheological behavior of the fresh paste being the main critical issue [19–23]. On the other hand, powder-based

* Corresponding author. University of Padova, Industrial Engineering Department, Padova, Italy.
E-mail address: prof.hamada.elsayed@gmail.com (H. Elsayed).

https://doi.org/10.1016/j.oceram.2021.100162
Received 25 March 2021; Received in revised form 11 June 2021; Accepted 9 July 2021
Available online 22 July 2021

binder jetting does not have any significant restrictions in terms of shape choice, at the same printing time, but it has limitations in terms of part dimension which depend on the printing envelope of the specific printer employed. The main difficulties associated with this technology are the optimization of the flowability of the powders used to generate the individual layers of the powder bed and the approach used for the selective deposition of the liquid. A range of materials, such as traditional Portland or magnesium-based cement and geopolymers, were introduced in the powder bed as binders using different liquid systems [24–29].

Magnesium phosphate cements (MPCs) are commonly used in the stabilization/solidification of wastes, rapid repairing of industrial and civil structures, and 3D printing of scaffolds for biomedical applications [30–32]. In the first studies, mono ammonium phosphate (MAP) was generally used, with the drawback of ammonia release during reaction and the generation of very high heat. For this reason, mono potassium phosphate (KH_2PO_4, MKP) is now prevalently used, with additional benefits in terms of heat release and setting time. Similarly to other traditional cementitious materials, the magnesia to phosphate molar ratio (M/P), the water to binder ratio (w/b), the reactivity of the magnesia, the fine aggregate to binder ratio and the use of retarders are the key parameters affecting the results. Theoretically, the largest amount of the desired reaction product is obtained with a M/P molar ratio of 1. However, in most of the studies the M/P ratio used is much higher than that, and generally with a M/P ratio between 3 and 8 higher mechanical properties and better durability are reached [33–35].

The microstructure of a 3D printed component is directly related to its final properties as well as to the quality of the manufacturing process employed in its fabrication. The microstructure of a part is usually characterized by optical (OM) and/or Scanning Electron Microscopy (SEM), which provide 2D information from the surface of the sample. Successive sectioning and additional microscopy investigations are needed to evaluate the entire 3D microstructure. X-ray Computed Tomography (XCT) is a non-destructive technique capable of investigating the internal structure of a part [36,37]. Numerous studies focused on the relationship between microstructure and mechanical properties. XCT has been, for instance, employed to evaluate the influence of defects on the flexural strength and to study, *in-situ*, the damage mechanisms in ceramic materials [38–40]. XCT is also been increasingly used to investigate AM processes [41–43], or to assess the geometry of the produced parts and characterize their microstructure [44–47].

This work aimed at studying and validating the large-scale AM of artificial stone components by Binder Jetting, using a sustainable magnesium potassium phosphate cement as a binder. The printing bed was comprised of aggregates, reactive magnesium oxide (MgO) and mono potassium phosphate (MKP) particles, and the binder reaction was activated by the selective deposition of water. In order to better understand and control the different phenomena involved in AM by the binder jetting technique using a reactive powder bed, XCT characterization was carried out at successive steps of the process: powder bed generation, binder activation and after the part has been formed. Our objective was in particular to investigate the heterogeneities created during the printing steps and to potentially identify their origin, as these can significantly affect the performance of the printed parts. The influence of the voxel size on the part's characteristics was assessed by comparing printed components produced using two different printers.

2. Materials and methods

2.1. Materials

The printing powders were prepared by mixing magnesium oxide (MgO, CCM grade, RHI Magnesita GmbH, Vienna, Austria, with the particle size distribution shown in Fig. 1a) and mono potassium phosphate (KH_2PO_4, MKP, agricultural grade, Agri 2000 Italia srl, Ferrara, Italy, with a particle size >2 mm, as shown in Fig. 1b) with different aggregates. It should be noted that MKP had a particle size >2 mm when used in the large printer, while it was ground to a size >0.5 mm when used in the small printer.

Local river sand with a particle size distribution between 0 and 2 mm (Bacchi spa, Boretto (RE), Italy) was used as unreactive aggregate, and in one formulation porous glass particles with a particle size distribution between 0.25 and 1 mm (Dennert Poraver GmbH, Schlüsselfeld, Germany) were added as lightweight aggregate. The powder bed feedstocks were obtained by mixing all the powders in a concrete mixer for 20 min, reversing the inclination of the drum at half-time. A good homogenization was observed after discharging the powders, and no crushing of the aggregates was noticeable. Tap water, selectively jetted through the nozzles in the printer head, was used as the liquid activating the binder ($MgO + KH_2PO_4$). The different formulations of the powder bed feedstocks are reported in Table 1. The water to binder molar ratio was 0.4, while the M/P molar ratio was 3.38, which is consistent with literature data for concrete [33–35].

The bulk density was calculated following normative EN ISO 60, and true density was theoretically calculated using the value reported for the

Table 1
Powder bed formulations.

Mix	Reactive binder powders (wt%)		Aggregates (wt%)	
	MgO	MKP	Sand	Poraver
Mix1 *(sand mix)*	16.7	16.7	66.6	0
Mix2 (*Poraver mix*)	22.6	22.6	45.3	9.5

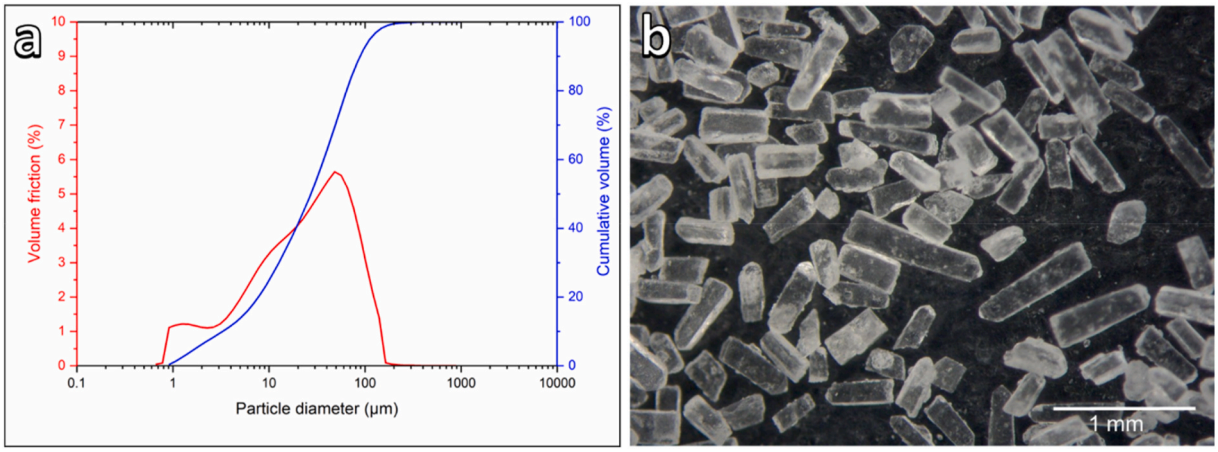

Fig. 1. a) MgO particle size; b) KH_2PO_4 (MKP) crystals.

raw materials: sand 2.6 g/cm^3, MgO 3.3 g/cm^3, MKP 2.34 g/cm^3 and Poraver 0.60 g/cm^3. The solid packing factor (PF) of the different mixes was determined to be 57.20% (sand mix) and 42.20% (Poraver mix). In the Poraver mix, the fact that Poraver spheres have their own "internal" porosity (open and closed) that affects the packing factor value, was considered. Typically, good packing values are between 0.5 and 0.7, and the packing factor depends on particle shape, particle size distribution, the interaction between particles and external process factors such as the way the particles are supplied from the hopper to form the powder bed layer, the way the blade flattens such layer before printing, the application of pressure or vacuum on the deposited powder layer, etc.

2.2. Printing process

Two different printers were used (Desamanera Srl, Rovigo, Italy); they adopt the same production process but with differences in the maximum dimension of the printed sample (60 × 60 × 60 cm^3 vs 150 × 150 × 150 cm^3 for the small and large printer, respectively) and the fabrication voxel dimension (minimum volume in which the object to be printed is subdivided, ideally corresponding to the minimum volume of the powder bed filled by the printing liquid). Both printers use a recoater for laying down each powder layer, which deposits a certain volume of the desired layer (70 and 50 vol% for the large and small printer, respectively) when moving forward. Then, the printer head attached to it moves backward, jetting liquid in selected areas of the layer and the recoater follows it depositing the remainder of the powder layer. The printer with the smaller printing envelope (Desa1 60.60), with which the research was carried out at the University of Padova, has a cubic voxel resolution of 3.0 × 3.0 × 3.0 mm^3. The larger printer (Desa1 150.150), located at Desamanera's headquarters, has a cubic voxel resolution of 5.7 × 5.7 × 5.7 mm^3 (see Fig. 2a and Fig. 2b, respectively).

The printing process started with the preparation of the printing bed, depositing the powder in x-y plane (Fig. 2c). The printing head, after being raised in the z-direction of the preset percentage of the layer, selectively deposited water through 192 or 264 nozzles (small and large printer, respectively) with an internal diameter of 1.1 mm, where desired, to activate the binder reaction. Then, the recoating system, after rising in the z-direction of the preset percentage of the layer, immediately deposited new powder mix, creating a new pristine layer to be inscribed by the printing head. The process was repeated until the number of total layers was complete. The printed pieces were left in the powder bed for at least half an hour, at room temperature, before being extracted, and cleaned (Fig. 2d). The sand mix powder bed formulation was used with both the large and small printer, while the Poraver mix was used only with large printer. The amount of water jetted through the nozzles was 0.036 g/voxel and 0.0054 g/voxel (large and small printer, respectively), and the printing speed adopted was 50 mm/s.

2.3. Characterization of the physical and mechanical properties of the printed parts

The phase assemblage of printed samples was investigated, using a Bruker D8 advance X-ray diffractometer (Cu(kα), 10–70°, 0.05°/step, 2 s/step). The XRD pattern was analyzed with the software "Match!", supported by the PDF-2 database.

The flexural strength was measured on printed bars with a dimension of 30 × 30 × 135 cm^3 and, after testing, the fragments were cut with a diamond saw to obtain cubes of 30 × 30 × 30 cm^3 for compression tests. At least 5 samples per type were tested, using a universal testing machine (Galdabini Quasar 25) operating with a controlled head-speed of 0.5 mm/min. The samples were tested after 28 days from the printing, during which time they were kept at room temperature in air.

An optical microscopy (Stemi 2000-C with AxioCam ERc 5s) was used to evaluate the general morphology of the printed parts and to

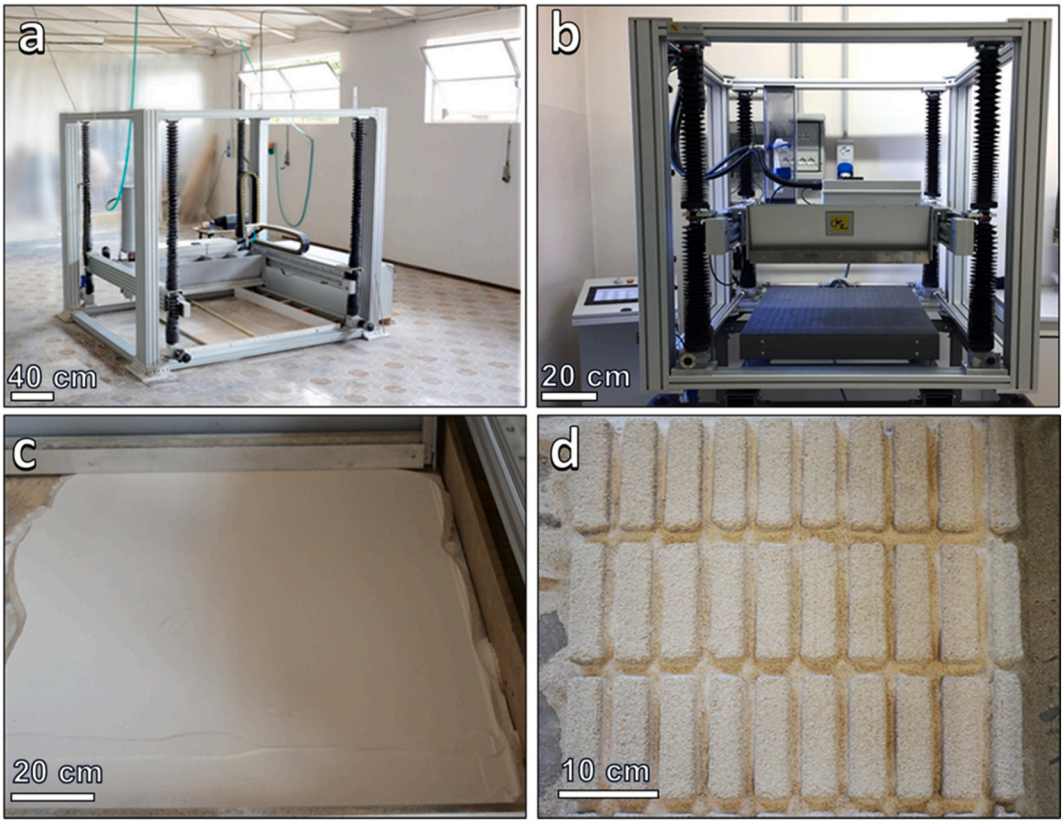

Fig. 2. a) large Desamanera printer (Desa1 150.150); b) small Desamanera printer (Desa1 60.60); c) Powder bed layer ready to be selectively inscribed with water; d) pieces partially extracted from the powder bed (images courtesy of Desamanera).

compare the microstructure of the samples printed by the small and large printers.

The bulk density was obtained by dividing the weight of fabricated samples by their volume measured using a digital caliper. The apparent and true density of the samples were measured by means of a gas pycnometer (He, Micromeritics AccuPyc 1330, Norcross, USA). The open and total porosity of the printed parts were then calculated as the ratio between their bulk, apparent and true density values.

2.4. Three-dimensional imaging using X-ray microcomputed tomography

To better understand the reactive binder jetting process, X-ray computed tomography (CT) was used for imaging the powder bed, monitoring *in situ* the hydration reaction and visualizing interior features of the printed objects as well as obtaining digital information on their 3-D geometry and porosity.

2.4.1. Specimens' preparation for X-ray microcomputed tomography

Powder samples were collected from the dry powder bed of the large printer in order to detect stacking heterogeneities linked to the recoater deposition. For this purpose, a plastic cylindrical box, of inner diameter of 55 mm and height of 35 mm, was used to collect the powder. The box was inserted on top of the powder-bed and blocked at the bottom with a thin plastic sheet; then, the box was extracted from the bed, turned upside down and closed with a lid. A comparison was made with a random stack obtained by pouring manually powder into a container of a size close to the one used to collect the powder deposited by the recoater.

For X-ray tomography observation of the hydration reaction, dry powder was randomly poured into a cylindrical container with an inner diameter of 12 mm. This container was placed inside the tomograph and water was deposited manually on top of the powder bed in the cylinder using a VWR Pasteur pipette 7 ML. Based on 15 tests with a precision balance, the quantity of water was estimated at 0.043 ± 0.0035 g (compared to 0.036 g/voxel for large printer). Therefore, the quantity of water was not exactly the same as the one delivered by the printers, but very close to it.

Pieces of the printed bars and cubes, as described in Table 2 and shown in Fig. 3, were analyzed by means of X-ray tomography.

2.4.2. Acquisition of X-ray microcomputed tomography data

Three-dimensional observations of the materials before, during and after hydration were carried out by means of X-ray tomography using a vtomex device (GE Phoenix | X-Ray GmbH) equipped with a 160 kV nano-focus tube, a tungsten transmitting target, and a 1920 × 1536 pixel Varian detector (see Buffiere et al. [48] for more details). The X-ray tube produces a polychromatic conical beam. The experiments were performed with various parameters depending on the sample features (thickness, attenuation, resolution needed) and time restrictions, see Table 3.

Powder collected after the deposition from the recoater and powder randomly poured were scanned using a continuous rotation to avoid particles movement during scanning. Since the aim of the investigation was to assess the density heterogeneity, a large field of view was preferred rather than a high resolution, and an imaging voxel size (volume element or 3D pixel) of 35 μm was used. Due to the size of the samples, a voltage of 150 kV with a 0.5 mm thickness copper filter was necessary to obtain sufficient transmittance.

Concerning the setting reaction, the acquisition parameters were optimized in order to reduce the scan time and thus follow the fast evolution of the microstructure. A continuous rotation was used, and the integration time was 200 ms for each of the 1000 projections acquired over 360°. These parameters resulted in measurement periods of 200 s for a complete scan. The initial (dry state) and final states (at the end of the reaction) were acquired with improved conditions, *i.e.* an exposure time of 333 ms and 3000 projections. For the printed samples, the voltage was adjusted depending on their size; a slow acquisition, a step-by-step rotation and an averaging of 5 images at each angle were used. This reduced the noise in the images and thus facilitated the quantification of the features of interest.

Using a Filtered Backprojection algorithm, the series of radiographs were combined to reconstruct a 3D digital image where each voxel represented the X-ray absorption at that point.

2.4.3. X-ray microcomputed tomography images analysis

At the end, the reconstructed data were processed and visualized with the public domain ImageJ/Fiji shareware [49,50]. Reconstructed 2 slices extracted from the volume were presented with different orientations for qualitative purpose. Slices according to the x-z plane corresponded to views parallel to the vertical axis, with the surface where powder or water were deposited located at the top. Slices according to the x-y plane, perpendicular to the vertical, will also be shown later. These slices were extracted from areas with different densities in order to highlight heterogeneities in the samples. In these images, pores appeared dark with low grey level values, due to the weak X-ray absorption, while areas of higher attenuation (e.g. sand particles) appeared brighter.

Some heterogeneities were not easy to highlight on a single 2D slice; to overcome this issue, projection methods were applied. The Z project function of ImageJ can be applied to an image stack in order to determine for each pixel the minimum or the sum within the stack along each column of voxels. This was a way to project the complete information of the stack into a 2D image. For the powder data, a minimum function was used because the variations were small. For printed specimens, a sum function was more suitable because the amount of porosity was much higher.

A segmentation process was applied in order to separate all the voxels of the image into two families (black and white), which will hereafter be considered as belonging to the solid phase and the pores. Based on this, 3D rendering was obtained by drawing a surface between all the voxels exhibiting the same grey level.

From the binarized volumes, it was also possible to quantify the different features. The simplest characterization was to measure the density, by calculating the proportion of voxels belonging to the solid phase or to pores. Because the tomographic data describe the three-dimensional structure, profiles of density calculated in slices as a function of the position of each slice were also created. This analysis was carried out along different directions (parallel or perpendicular to the vertical axis, which was also the printing direction). For statistical reasons, the average of the surface fraction over a sufficient number of this kind of slices is equal to the average fraction of porosity over the entire volume.

The "local thickness" plugin [51] was used to calculate the pore size. The local thickness is defined as the diameter of the largest sphere that fits inside the object. It can therefore be considered as the smallest lateral dimension of the object. A homemade plugin was used to measure the connectivity of the porous network. Connectivity is defined as the ratio of the largest porosity area to the total porosity.

Table 2
Printed samples analyzed by means of X-ray tomography.

Sample	Printer	Powder bed formulation	Sample size (*L, H, W*), mm
S1	Large printer	Sand mix (sample 1 in Fig. 3)	41, 42, 79
S2	Small printer	Sand mix (sample 2 in Fig. 3)	28, 36, 64
S3	Large printer	Poraver mix (sample 3 in Fig. 3)	28, 36, 64

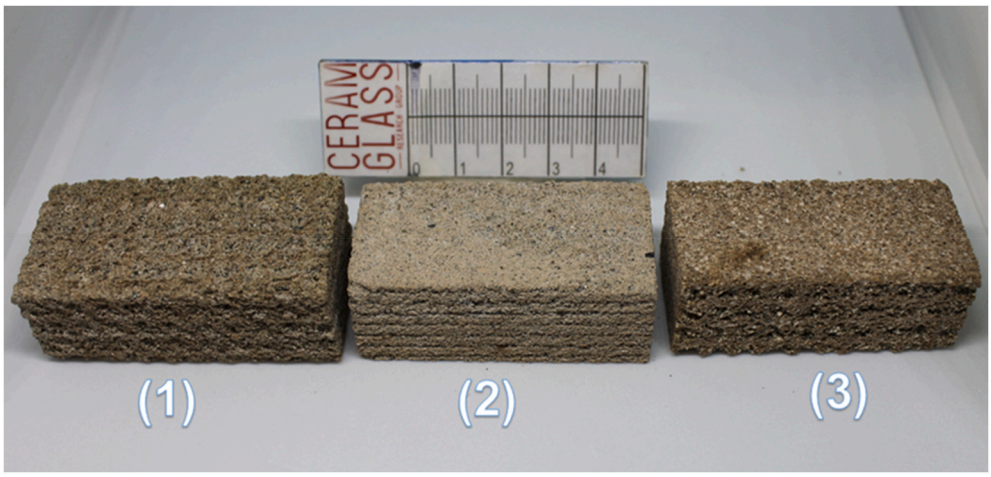

Fig. 3. The printed samples analyzed by means of x-ray tomography. (1) Large printer, sand mix - S1; (2) Small printer, sand mix - S2; (3) Large printer, Poraver mix - S3.

Table 3
X-ray tomography acquisition parameters used to investigate the dry powder bed, the setting reaction and the printed samples.

Parameter	Sample type		
	Dry powder bed	Setting reaction	Printed samples
X-ray source voltage (kV)	150	80	80 - large printer (Mix2) 120 - small printer (Mix1) 140 - large printer (Mix1)
Filter	0.5 mm copper foil	no	no - large printer (Mix2) 0.1 mm copper foil - small and large printer (Mix1)
Current (μA)	60	350	260 - large printer (Mix2) 120 - small printer (Mix1) 80 - large printer (Mix1)
Exposure time (ms)	500	200 - fast scan 333 - slow scan	333 - large printer (Mix2) 500 - small and large printer (Mix1)
Number of projections	4000	1000 - fast scan 3000 - slow scan	1500
Voxel size (μm)	35	5	15
Acquisition mode	Continuous without averaging	Continuous without averaging	stepwise with an average of 5 radiographs for each projection
Acquisition time (s)	2000	200 - fast scan 990 - slow scan	3000 - large printer (Mix2) 4500 - small and large printer (Mix1)

3. Results and discussion

3.1. Physical and mechanical characterization of the printed parts

The main consolidation product of the magnesium potassium phosphate cement (MPC) is K-Struvite ($MgKPO_4{\cdot}6H_2O$). The hydration and precipitation process are based on an acid-base reaction, with the fast dissolution of acid MKP crystals and the subsequent reaction with MgO powder, mainly controlled by the pH which regulates the oxide dissolution. The process follows the main reaction:

$$MgO + KH_2PO_4 + 5H_2O = MgKPO_4{\cdot}6H_2O \quad \text{Eq. 1}$$

Nevertheless, the mechanisms that control the formation of the consolidated phase in MPC are not yet entirely known and still under investigation. Several mechanisms of homogeneous nucleation, heterogeneous nucleation, multiple precipitation/dissolution reactions with different final products in terms of composition, have been proposed [52–58].

The XRD patterns, reported in Fig. 4, confirmed the formation of K-Struvite as the binding phase in the 3D parts printed with the sand mix formulation, testifying the effectiveness of the printing procedure [54]. In addition, the complete disappearance of MKP and the presence of a small residue of MgO can be observed, due to its excess in the initial composition.

Fig. 5 shows optical images collected from the printed parts, after cutting with a diamond saw. We can observe that the water jetting created evident grooves in the powder bed, as visible in Fig. 5b, d and 5f. These contributed to the creation of a weak interface between layers and the development of high and low density areas. The impact of the holes created by the water droplet was reduced in samples produced with a smaller voxel size. The interfaces between the layers appear to be homogeneous, with layers regularly spaced depending on the voxel size. The holes created by the water droplets were also regularly spaced, in the X, Y and Z axis, at intervals of ~3 mm (corresponding to the voxel size of the small printer; Fig. 5b) and of ~5.7 mm (corresponding to the voxel size of the large printer; Fig. 5d and f).

The presence of macro porosity concentrated at the interface between layers caused inhomogeneity in the microstructure, increasing the local and total porosity and decreasing the overall mechanical strength of the printed parts. The mechanical and physical properties are reported in Table 4. The samples printed with the small printer possessed a flexural strength of ~2 MPa and compressive strength of ~2.7 MPa, while the samples printed with large printer possessed lower strength and higher total porosity. Regarding testing along two different orthogonal directions to the printed layers (perpendicular (XY-direction) and parallel (Z direction)), a similar value was found for the flexural and compression strength of the samples, independently on the printer used. This suggests that, despite the observed high porosity interface between the layers, the overall mechanical behavior of the parts was not affected, while the size of the grooves produced by water impact affected the total porosity hence the strength of the samples. We should point out, nevertheless, that in samples tested parallel to the printing direction the fracture propagated preferentially along the layer interfaces, indicating the presence of a weak region between each layer, while this was much less evident when testing perpendicularly to the printing direction.

We can observe that the ratio of compressive strength to flexural strength is up to almost 1:1 for the studied binders. From the experimental results, Chen et al. [59] reported that the ratio between

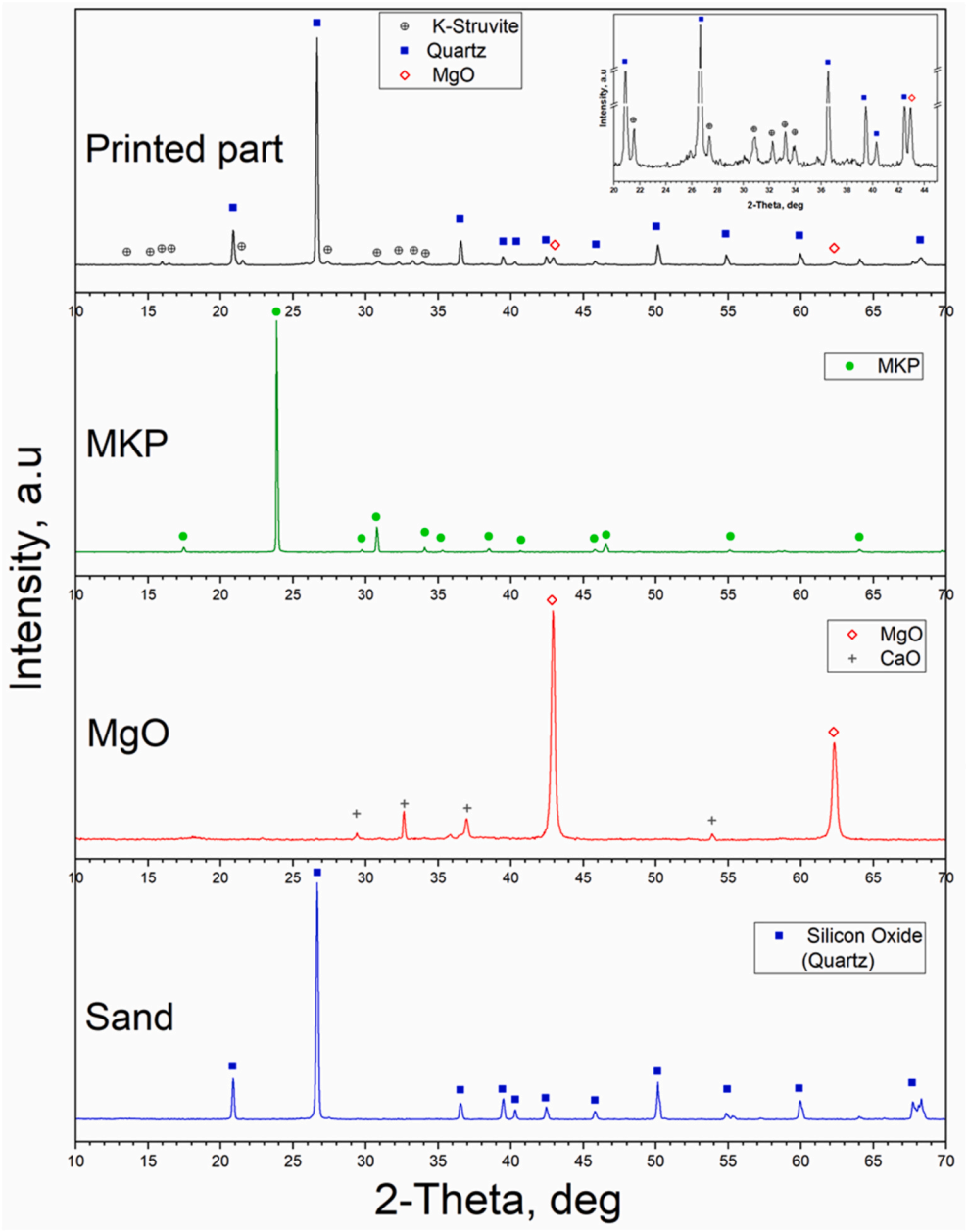

Fig. 4. XRD patterns of raw materials and of a printed part (sand mix powder bed formulation).

compressive strength and flexural strength, of cement mortar, was higher than 1:1; however, the ratio could be varied and was mainly influenced by the porosity of the developed parts. In addition, we have a varied porosity in our 3D printed parts, and this could also affect the results (i.e. the ratio). Specifically, the porosity is higher and more localized between printed layers, with larger pore sizes with respect to the rest of the material, as shown in Fig. 5. More studies are necessary to further explore the role of the amount of porosity on the compressive strength and flexural strength of the printed parts.

We can conclude that the fabricated samples, produced with the Sand mix and Poraver mix, possess suitable mechanical properties (1.7–2.4 MPa and 1.6–2.8 MPa for the flexural and compression strength, respectively), with a porosity varying between 40 and 54 vol%. This material is competitive with non-structural concrete and porous stones [60–63], and it has in addition all the advantages deriving from the AM technology in terms of design flexibility and process constancy.

3.2. *X-ray microcomputed tomography analysis of the dry powder bed*

Local tomographies (i.e. field of view smaller than the sample size) were performed on the powder samples (sand mix*)* with a voxel size of 35 μm which allowed to image a volume of 35 × 35 × 35 mm^3 inside larger samples. Fig. 6 shows reconstructed slices according to the XZ plane, parallel to the vertical axis, for the powder bed obtained with the large printer (Fig. 6a) or by randomly pouring the powders in the container (Fig. 6b). Sand or binder particles can be seen in bright color, while pores appear in dark color. No large heterogeneities are visible in these 2D slices. Projections of the minimum intensity of each pixel through the stack are shown in Fig. 6c and d. Dark areas, related to areas with lower density, were observed in both cases. A more regular spacing can be observed in the case of the powder deposited by the recoater, and the distance between these layers was of the same order of magnitude as the voxel size of the printer (i.e. 5-6 mm).

Fig. 7 shows the profiles of the evolution of the large cavities fraction

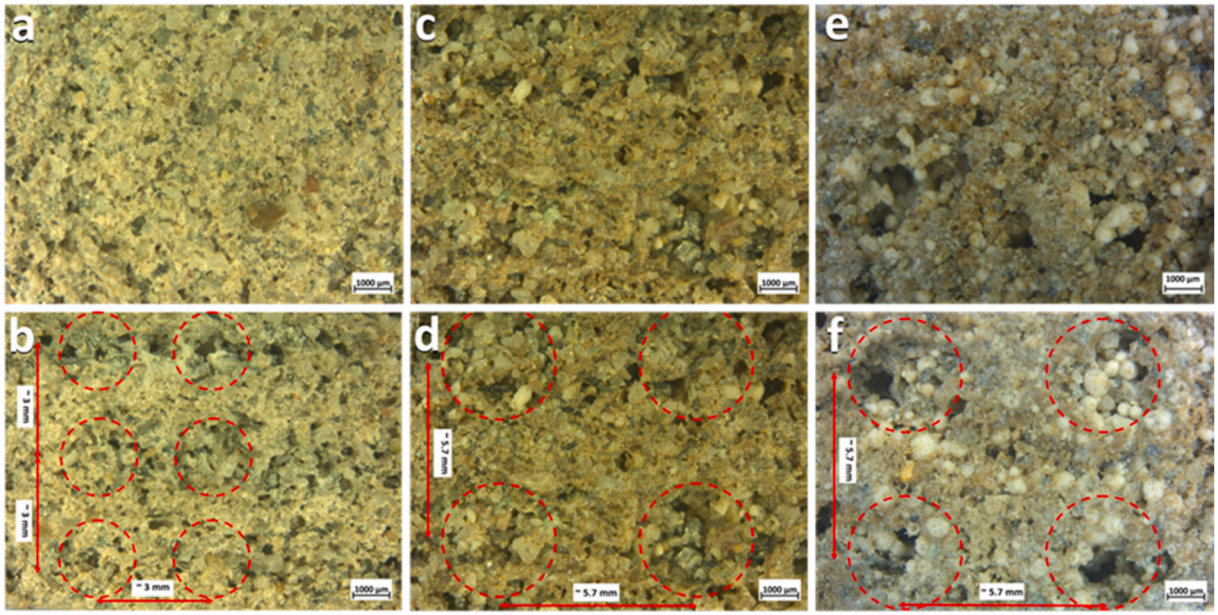

Fig. 5. Optical images of printed parts: a) top and b) side view of sand mix printed using the small printer; c) top and d) side view of sand mix printed using the large printer; e) top and f) side view of Poraver mix printed using the large printer (the Poraver particles appear as white in the image). Holes created by the water drop are highlighted by the red circles. (For interpretation of the references to color in this figure legend, the reader is referred to the Web version of this article.)

Table 4
Physical and mechanical properties of the printed parts; the mechanical properties were tested parallel (XY direction) and perpendicular (Z direction) to the printed layers.

Formulation/Printer	Bulk Density (g/cm^3)	Open porosity (vol%)	Total porosity (vol%)	Flexural strength (MPa)		Compression strength (MPa)	
				XY direction	Z direction	XY direction	Z direction
Sand mix/small printer	1.49 ± 0.01	39 ± 1	40 ± 1	2.01 ± 0.27	2.38 ± 0.34	2.71 ± 0.72	2.80 ± 0.66
Sand mix/large printer	1.40 ± 0.02	44 ± 1	45 ± 1	1.76 ± 0.35	1.70 ± 0.15	1.60 ± 0.22	1.86 ± 0.28
Poraver mix/large printer	1.16 ± 0.02	48 ± 2	54 ± 2	2.30 ± 0.27	2.24 ± 0.31	2.27 ± 0.21	2.30 ± 0.81

of the dry powder bed (sand mix) generated along the vertical Z axis. With a voxel size of 35 μm, only areas with sufficiently large cavities could be taken into account after thresholding. These measurements do not allow precise measurement of the total porosity of the powder bed but confirm the presence of lower density layers regularly spaced, every 5–6 mm, in the case of powder deposited by the recoater of the large printer. Variations are quite small, and could be attenuated by the method of powder collection and transfer to the tomography system. However, the comparison with random pouring of the powder and the regular spacing in the case of the recoater deposition indicates that the deposition process indeed has an influence on the residual porosity present in the powder bed.

3.3. X-ray microcomputed tomography analysis of the binder reaction

The monitoring of the two-part binder reaction was carried out using a powder container selected to obtain the best compromise between the resolution and the investigated volume. Due to the relatively small container size, a voxel size of 5 μm was employed, which allowed for a suitable visualization of the microstructure of the material. The analysis of a volume of 6 × 6 × 3.5 mm^3, located close to the powder surface, was carried out using local tomographies.

A first slow acquisition of the dry powder bed was carried out in order to have the best possible characterization of the initial state. A 2D reconstructed slice parallel to the vertical axis (XZ) is shown in Fig. 8a. Large particles, often several hundred microns in size, are observed in bright color, but the contrast obtained is not high enough to clearly differentiate sand particles from binder (MKP and MgO particles) by means of grey levels. The evolution of the particles during the reaction as well as their geometry will be the only way to differentiate them. The shape and dimension of the sand particles do not change with time, MgO particles react at their surface, while MKP particles are dissolved by water. The MKP binder particles have also a more clearly defined geometric shape, with different facets (see Fig. 1b). In Fig. 8a, three MKP particles of different size were surrounded with a white dashed line so their evolution with reaction time could be monitored. The dark area between the large particles is probably composed of a mix of small binder particles (MgO), sand and pores, which is not possible to properly characterize at this resolution.

A drop of water was then deposited on the surface of the powder and a series of 10 fast acquisitions (200 s) was recorded until the end of the binder reaction. Fig. 8b shows the result of a scan started 30 s after the water deposition. A very fast evolution of the microstructure can be observed in this slice. All the dark areas around the larger particles have disappeared (see inside the yellow circle), replaced by a porous matrix with higher grey levels. The darkest grey levels correspond to newly created pores. The particle surrounded by the second white circle now has a void along its borders, linked to a dissolution process. Close to the surface the changes are most pronounced, the position of the sand particle circled in orange has changed and it has moved closer to the surface. In the area surrounded in purple, isolated particles are now visible on the surface. Then, the microstructural evolution appears to be less pronounced, being mainly related to the dissolution of the largest MKP particles. Monitoring of particle changes suggests that the size has an influence on dissolution rate: the small particles, n° 3 and n° 2 circled in white, were totally dissolved after 1030 s, see Fig. 8c, unlike the larger

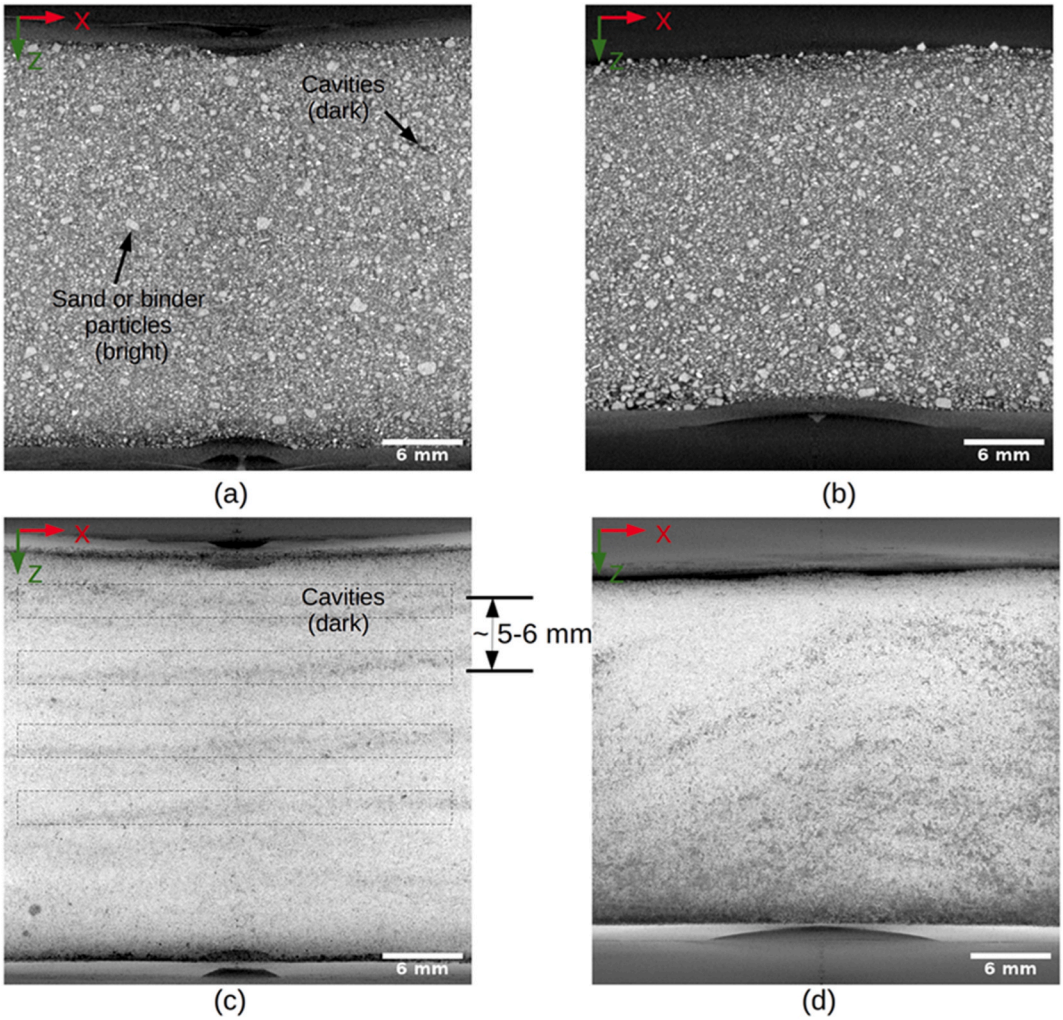

Fig. 6. XCT reconstructed 2D slices according to the XZ plane for the dry powder bed (sand mix) after: (a) deposition by the recoater (large printer) or (b) random pouring. 2D projection of the powder bed representing the minimum intensity (in the unsegmented image) of all slices along the Y axis after deposition by the recoater (c) or after random pouring (d).

particles, n° 1 in the white circle, which remained visible but with a reduced volume. The dissolved particle left a pore of shape and size similar to the initial binder particle, just like it was observed for plaster in previous research [64].

Finally, a slow acquisition was carried out 4200 s after the beginning of the binder reaction, see Fig. 8d. At this stage of the reaction, we can clearly observe that the large MKP particles have given rise to pores. It should be noted that some particles have not completely dissolved, as observed for particles n° 1 in the white circled area, with remaining portions visible in the other slices of the volume. A shell is visible in the dry state on some binder particles, and it does not evolve, being still present in the final state (particles n°1).

Reconstructed slices in the XY plane close to the surface, see Fig. 9, allow us to observe the effect of the water drop deposition. The same slice (same level) is shown for the same processing steps as in Fig. 8. In the dry state (Fig. 9a), a small amount of powder is only visible in a slice very close to the surface and parallel to it. In the slices at the same level but after water drop deposition (Fig. 9b and c), circularly arranged particles are now observed. In 2D, the particle arrangement looks like a ring, while in 3D it is rather like a small cup with a few particles inside. It should be mentioned, however, that the water drop was not exactly centered on the scanned area.

Close to the surface, large particles are the only ones remaining, as the water drop has probably dissolved and/or displaced the smaller ones. These large particles are separated by newly formed pores. Some portions of the set microporous matrix are, however, visible, as shown in the area circled in yellow (Fig. 9d). On the surface, once the drop of water has been deposited, microstructural changes are limited as it can be observed by following the evolution of the particle circled in blue linked to the partial dissolution of a MKP particle. The comparison between Fig. 10a and b showing isosurfaces of the solid part of the material clearly illustrates the new distribution of the large particles, with a significant amount now visible at the surface, after water deposition.

3.4. *X-ray microcomputed tomography analysis of the printed parts*

To evaluate the porosity network in the final products, the printed specimens were scanned by X-ray μ-CT with a voxel size of 15 μm and an analysis volume of 17.25 × 17.25 × 18.75 mm^3 (the field of view is smaller than the sample size). The microstructure of printed parts obtained using the small printer is shown in Fig. 11. A reconstructed slice, according to the XZ plane (Fig. 11a), shows a large amount of porosity. Projection of the sum for each pixel through the stack (Fig. 11b), confirms that there are large variations in terms of density. These areas of different density are regularly spaced at intervals of about 3 mm, which corresponds to the voxel size of the small printer. The slices realized in the high- and low-density areas illustrate these significant heterogeneities (Fig. 11c and d).

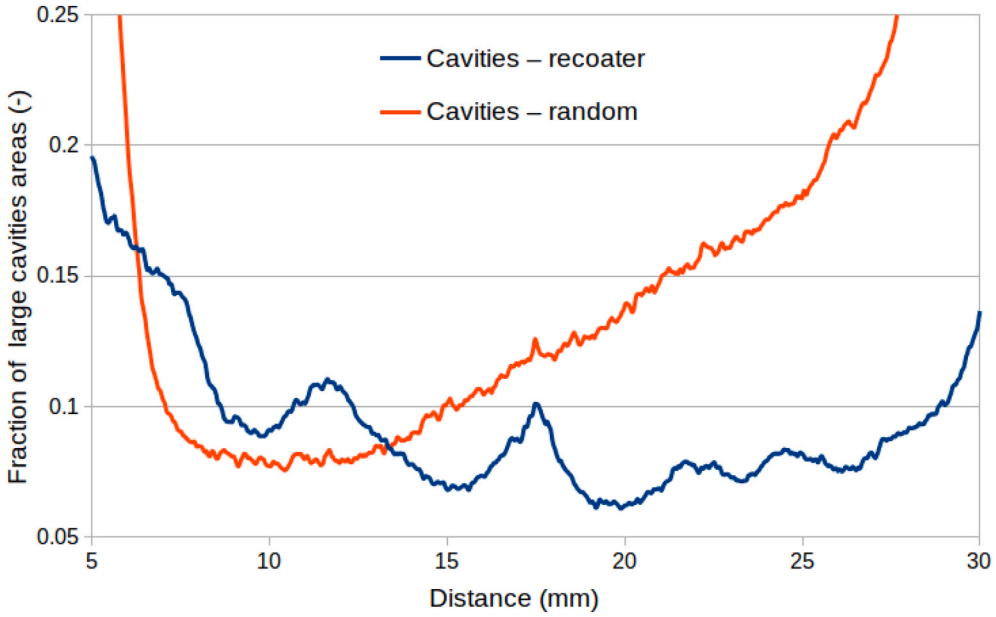

Fig. 7. Density profile of the dry powder bed (sand mix), along the Z axis (from top to bottom), after recoater deposition (blue curve, large printer) or after random pouring (red curve). (For interpretation of the references to color in this figure legend, the reader is referred to the Web version of this article.)

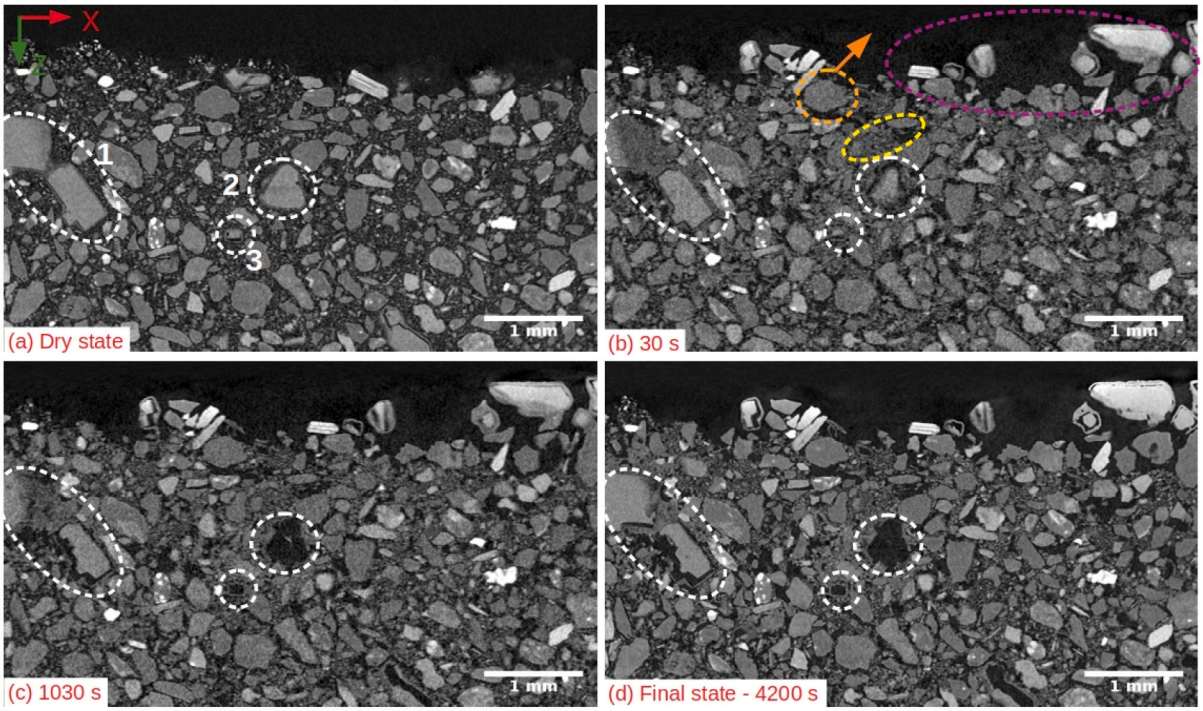

Fig. 8. Microstructural changes during the setting reaction. Reconstructed 2D slices in the XZ plane extracted from the bulk of 3D volumes acquired during the *in situ* tomography experiments: (a) dry state; (b) 30 s; (c) 1030 s; and (d) 4200 s after water deposition.

The microstructure generated by the large printer, also, presents a large amount of porosity, as it can be seen in Fig. 12a. High density regions can be observed in the projection of the sum for each pixel through the stack, Fig. 12b. They are separated by a value of about 5.7 mm, corresponding to the voxel size of the large printer. Lower density areas are located between high density ones. The pores found in this region appear to be more heterogeneously distributed compared to those present in the case of the sample produced using the small printer. Slices extracted from the lower density zone according to the XY plane, Fig. 12d, show features similar to the ones observed when following the binder reaction process. A pattern with circular shapes positioned approximately at a distance of 5.7 mm is visible, in accordance with the distance between the water drops deposited on the surface of the powder bed. Cracks are sometimes observed around these circular regions, and pores are also observed in the higher density area. By comparing their shape with observations made during the binder reaction, we can postulate that some of these pores derive from the dissolution of binder (MKP) particles. Indeed, they can possess a regular shape with facets, as

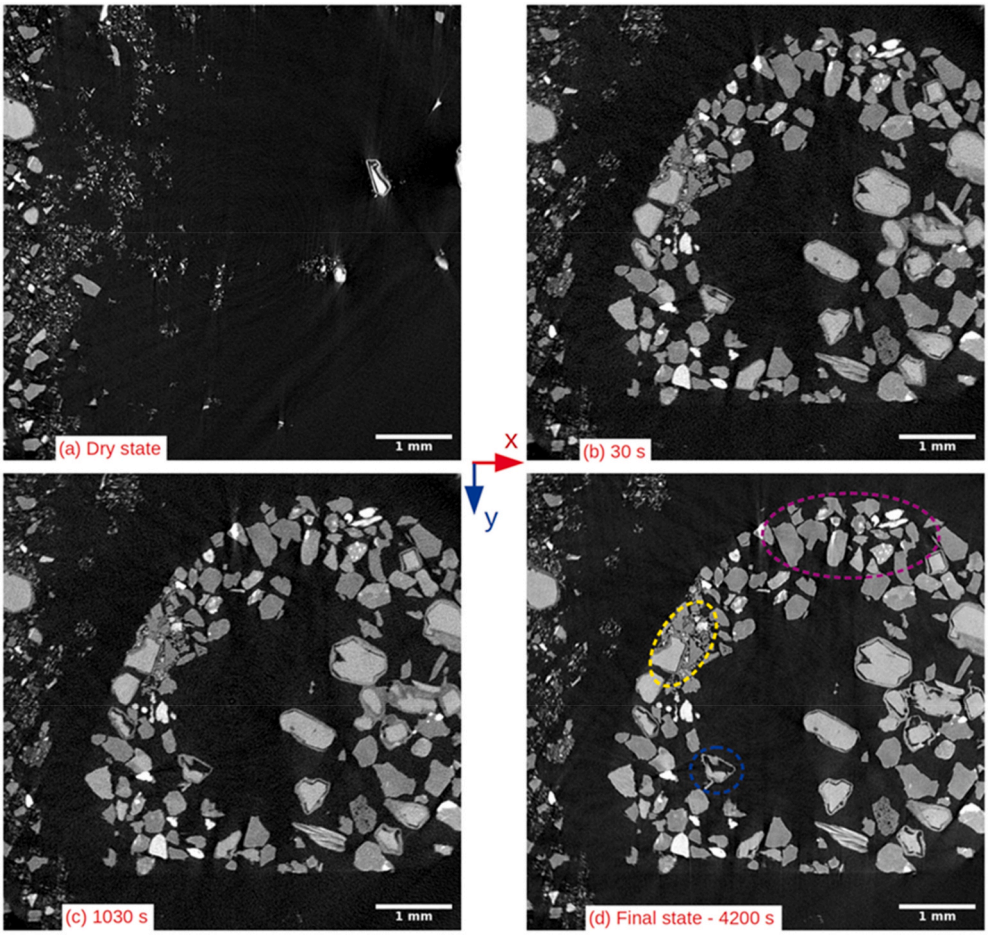

Fig. 9. Microstructural changes during the setting reaction: Reconstructed 2D slices in the XY plane extracted from the 3D volumes (close to the surface), acquired during the *in situ* tomography experiments. (a) Dry state; (b) 30 s; (c) 1030 s; and (d) 4200 s after water deposition.

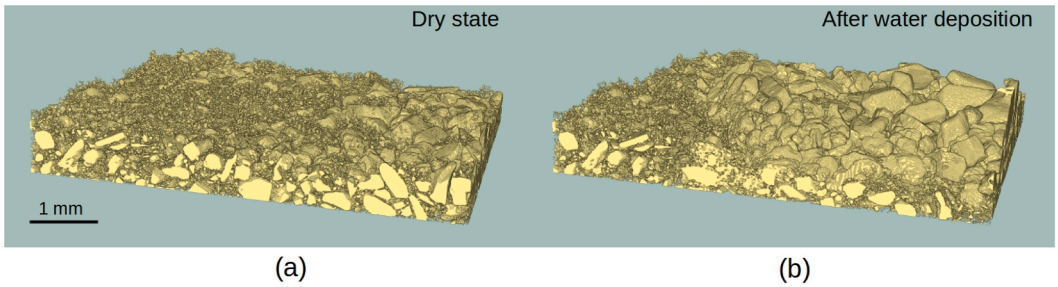

Fig. 10. 3D rendering of the powder bed; (a) dry state and (b) 4200 s after a drop of water has been deposited on the surface of the powder.

in the case of the pore surrounded in blue in Fig. 12c.

In Fig. 13, the density profiles calculated for parts printed by the small and large printers provide a quantitative evaluation of the differences between more or less dense regions. As expected, the profiles produced along the vertical Z-axis exhibit the most significant variations for both printers. The lowest density values observed are equivalent for both printers, being approximately 50%. The values measured in the densest zones are higher for the sample produced using the small printer, reaching about 85–90% compared to a maximum of 75% for the one produced with the large printer. The low and high density regions appear to be spaced by a distance compatible with each printers' voxel size. For the small printer, it is also interesting to note that this zone is divided by a thin layer of lower density, of about 70%. This is related to the layer thickness and fabrication voxel size as well as to the water droplet volume and smaller MKP particle size used in the case of smaller printer. The density profiles in the two other directions display no significant heterogeneities for the sample produced using the small printer, while more significant fluctuations are observed for the one produced using the large printer. The overall density is lower for the sample produced using the large printer, 62%, compared to 71.6% for the one produced using the small printer (Fig. 13). The differences between the total porosity measured by XCT and by pycnometry might be attributed to the presence of pores with a size below the adopted scanning resolution.

Connectivity measurements indicate that the pores are highly interconnected, as shown by the obtained values: 0.947 for the sample produced with the small printer and 0.993 for the one produced with the large printer. The pore size distribution, calculated from the segmented

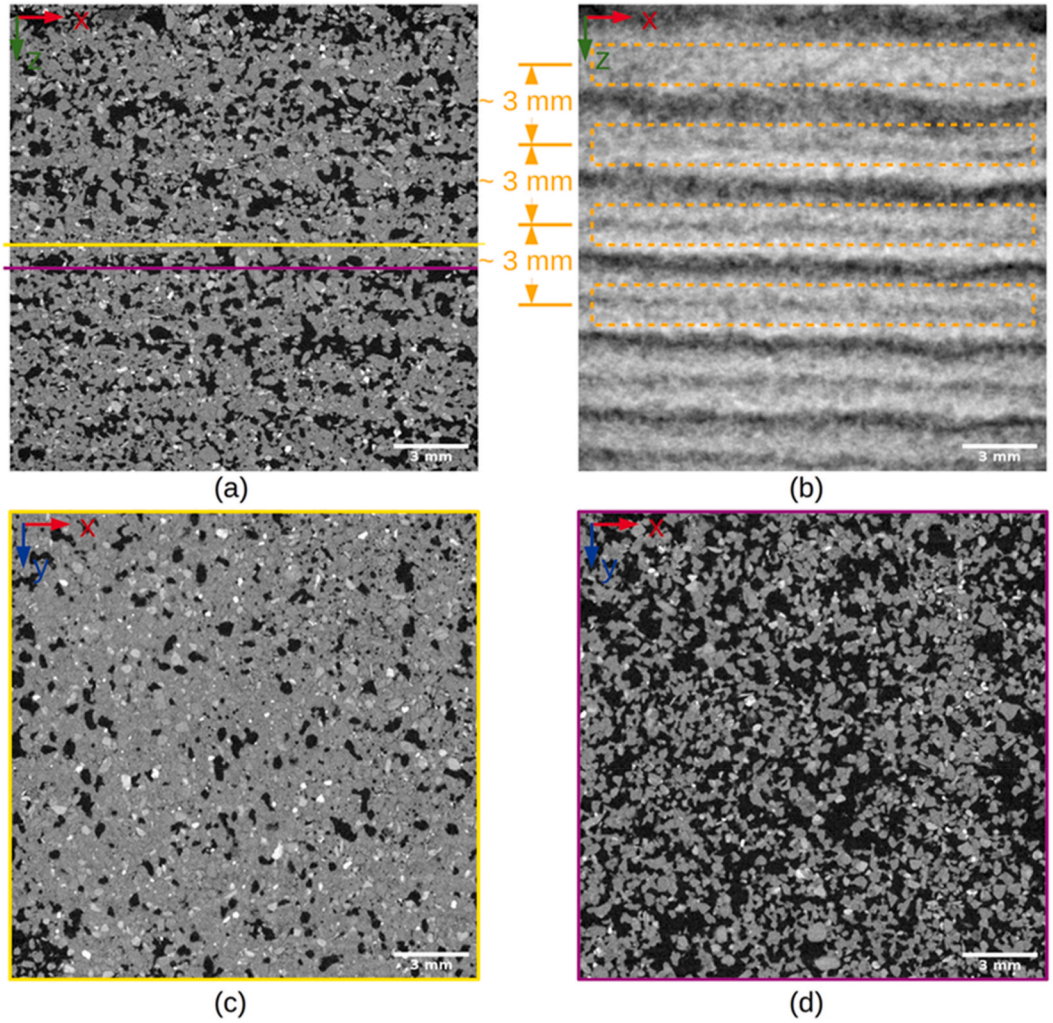

Fig. 11. Microstructure of printed part produced using the small printer: (a) reconstructed 2D slice according to the XZ plane; (b) 2D projection of the stack representing the sum of all slices along the Y axis; (c) reconstructed 2D slice along the yellow line in the high density zone; and (d) reconstructed 2D slice along the purple line in the low density zone. (For interpretation of the references to color in this figure legend, the reader is referred to the Web version of this article.)

tomograms using a digital granulometry (local thickness in ImageJ) is shown in Fig. 14. The maximum measured values are of 540 μm for the sample produced with the small printer and 960 μm for the one produced with the large printer. In the latter case, the size distribution is wider and a larger volume of small pores is also observed.

The same methodology was applied to assess the influence of the addition of lightweight Poraver particles to parts produced with the large printer, see Fig. 15. They appear with a grey level intermediate between that of the pores (black) and the matrix (light grey). The average size of these particles can be evaluated to be in the range of a few hundred of microns, in accordance with the information provided by the supplier. A large amount of porosity is present inside the particles, making the segmentation process and thus the precise size quantification very difficult. The observed microstructure is very heterogeneous, with denser zones composed of matrix, others presenting a large network of pores and finally some lightweight particle clusters (Fig. 15a). These heterogeneities are reflected in the projection of the sum for each pixel through the powder stacking, Fig. 15b, which is quite similar to the one observed in samples without lightweight particles, Fig. 12b. Reconstructed slices, in areas of different density, show the non-uniform distribution of lightweight particles and pores. Clusters of particles are more pronounced in a thin region located just below the high density zone, as seen on the left side of Fig. 15c. Just below the dense zone, large cavities, surrounded by matrix areas with a circular shape, are visible (right side of Fig. 15d).

The addition of lightweight particles appears to have increased the heterogeneity within the microstructure, as large fluctuations are visible in the density profiles along the vertical axis. This could be attributed to the fact that, when depositing the powder bed, they could partially segregate due to a density difference with the other constituents of the mixture (sand and binder particles). In Fig. 16, the density profiles corresponding to the matrix and lightweight particles are superimposed, and it is interesting to note that areas with higher lightweight particle density are located in the areas with the lowest matrix density. The average fraction of the matrix over the volume is equal to 38.7%, including sand as well as binder. The average fraction of lightweight particles is equal to 26%; however, this value is underestimated because internal pores could not be taken into account during grey level thresholding.

From the XCT data acquired on the powder bed generated by the recoater (Figs. 6 and 7), we can say that the existence of lower density regions separated by a distance comparable to the voxel size of the printer, i.e. the thickness of the powder layer deposited at each step, indicate that these were created during the fabrication process. These low density areas were also found in the printed parts, as shown in the reconstructed slices for samples produced using both the small (Fig. 11) and the large printer (Fig. 12). Moreover, the low density regions were more visible in the printed samples, especially the one produced with

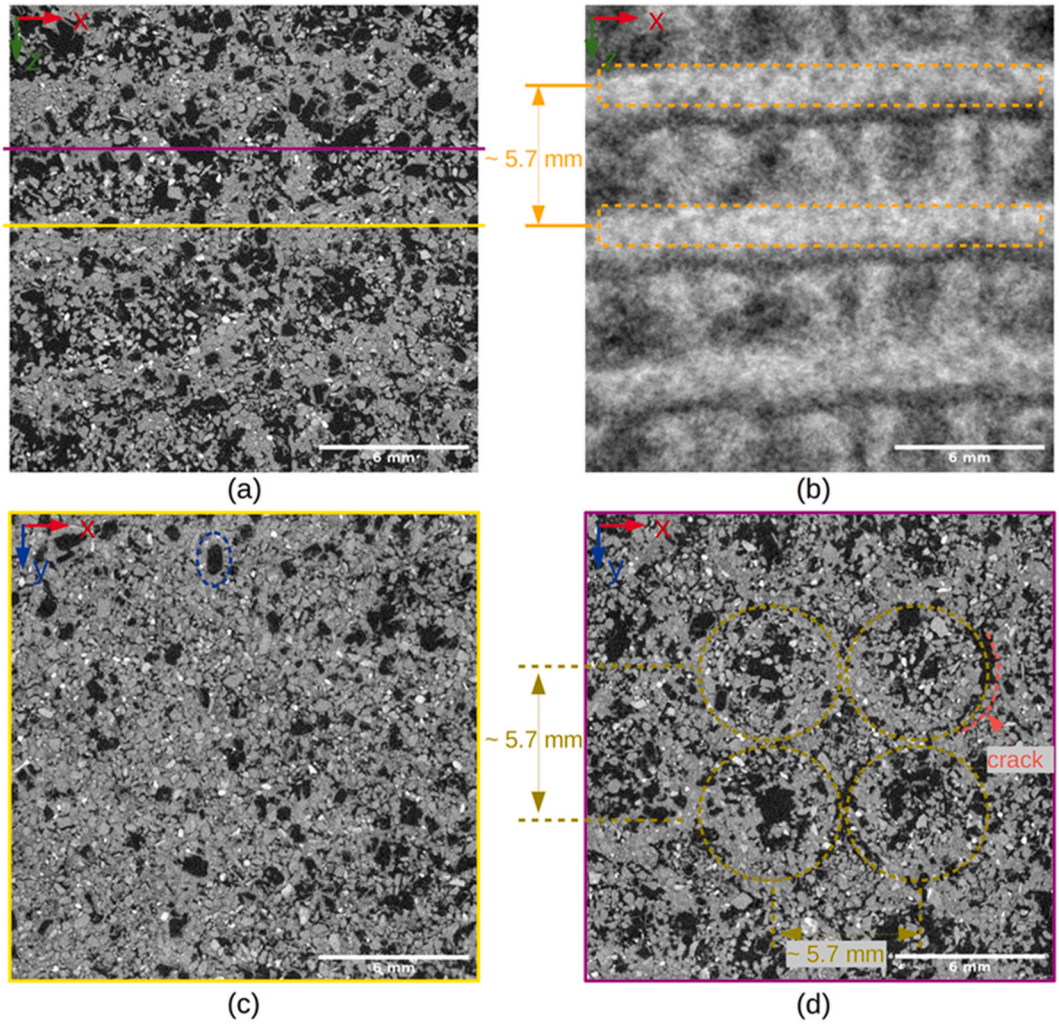

Fig. 12. Microstructure of the printed part produced using the large printer: (a) reconstructed 2D slice according to the XZ plane; (b) 2D projection of the stack representing the sum of all slices along the Y axis; (c) reconstructed 2D slice along the yellow line in the high density zone; and (d) reconstructed 2D slice along the purple line in the low density zone. (For interpretation of the references to color in this figure legend, the reader is referred to the Web version of this article.)

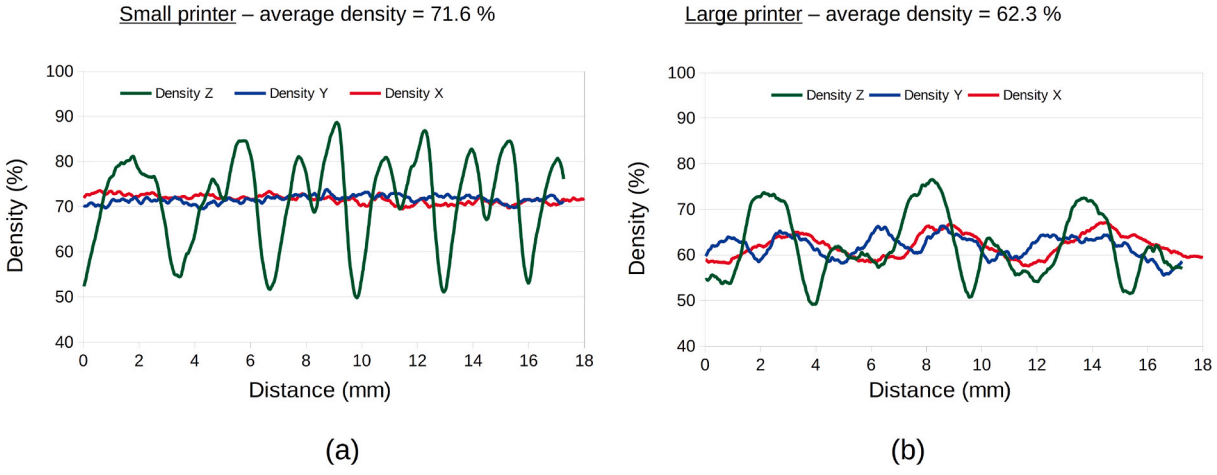

Fig. 13. Density profile of the printed parts along the XYZ directions: (a) small printer; (b) large printer.

the large printer, probably due to the effect of water deposition as well as MKP dissolution. In the case of printed parts produced using the Poraver mix, the distribution of lightweight particles also seemed to be influenced by the powder bed deposition, as layers of these particles were mainly located in the areas of lower density.

The deposition of a drop of water on the surface of the powder bed also affected the final microstructure, as demonstrated by the monitoring of the binder reaction carried out (see Figs. 8–10). Once the drop

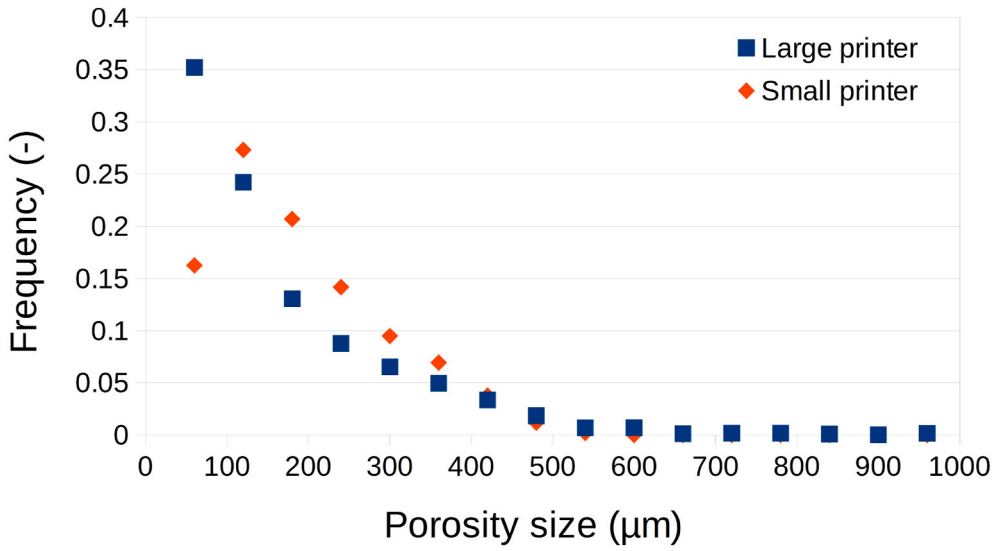

Fig. 14. The size distribution of pores, calculated using a digital granulometry (local thickness in ImageJ), for samples produced using the small printer (red color) and the large printer (blue color). (For interpretation of the references to color in this figure legend, the reader is referred to the Web version of this article.)

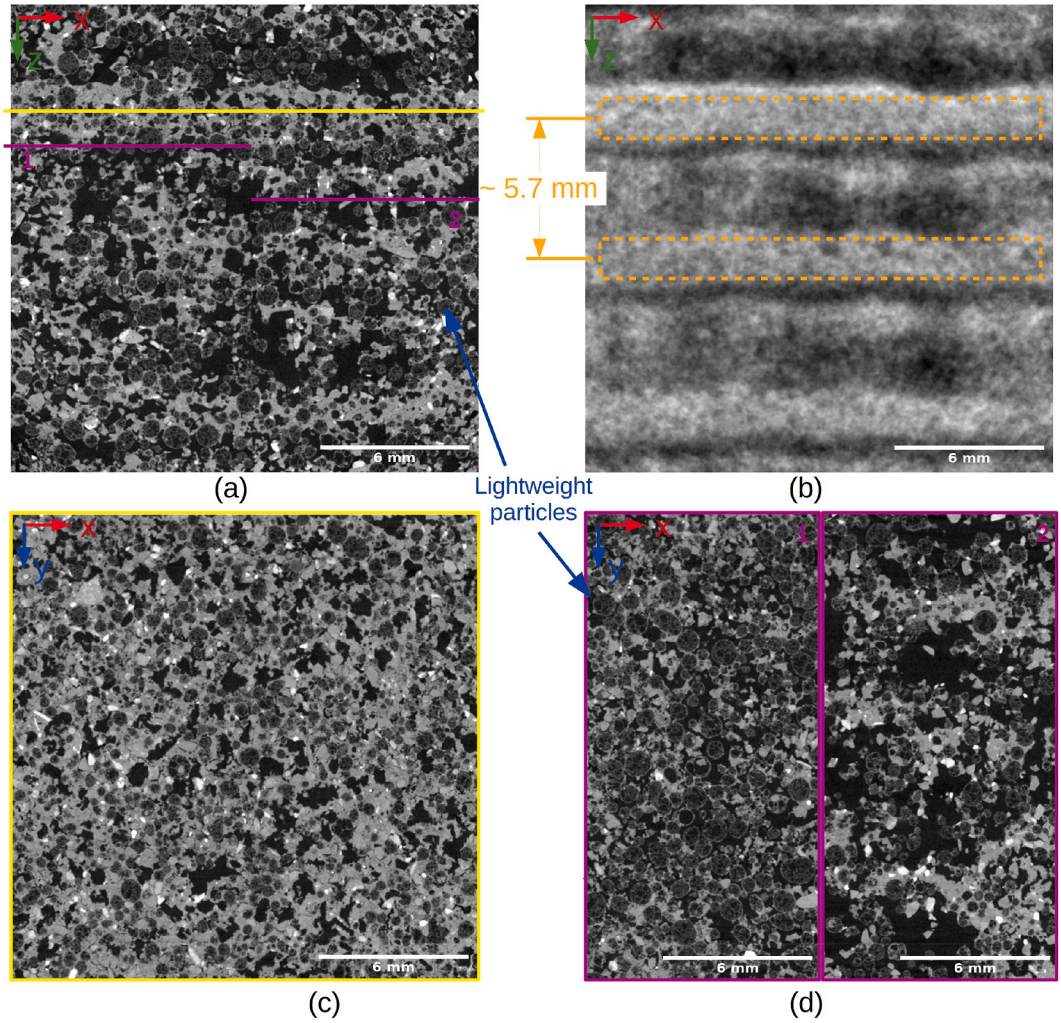

Fig. 15. Microstructure of a sample (Poraver mix) printed using the large printer: (a) reconstructed 2D slice according to the XZ plane; (b) 2D projection of the stack representing the sum of all slices along the Y axis; (c) reconstructed 2D slice along the yellow line in the high density zone; (d) reconstructed 2D slices along the two purple lines in the low density zone. (For interpretation of the references to color in this figure legend, the reader is referred to the Web version of this article.)

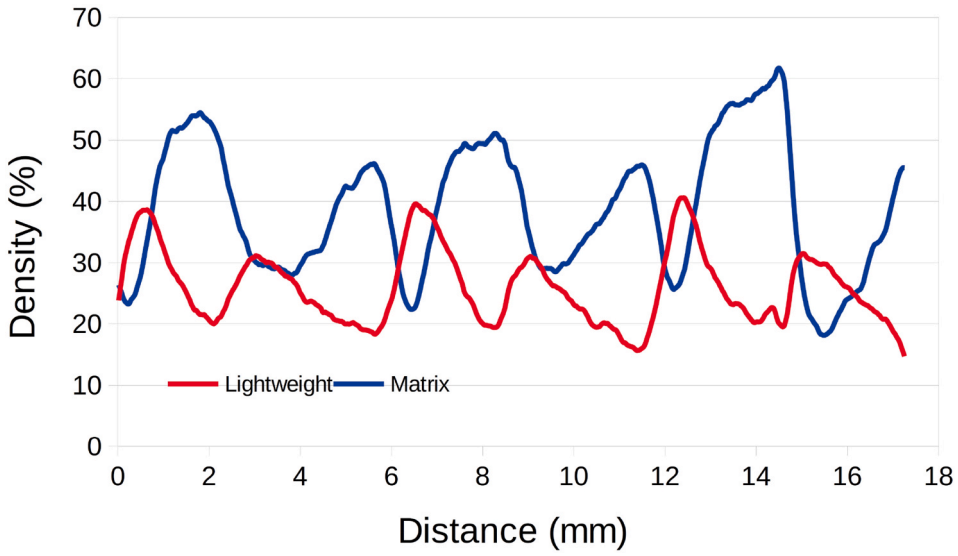

Fig. 16. Density profile along the Z axis for the matrix (sand + binder, blue line) and the lightweight particles (red line) of a sample (Poraver mix) printed using the large printer. (For interpretation of the references to color in this figure legend, the reader is referred to the Web version of this article.)

of water was deposited on the surface of the powder bed, binder and sand particles were redistributed, particularly at the surface, with many large particles clustering at the surface, creating additional porosity within the printed layer. A similar type of particle distribution was already observed with a high-speed camera in sand [65]. In our reactive powder bed system, the effect could also be due to both (partial) dissolution of the MKP particles, downward dragging of small MgO particles and/or the setting reaction between the two-part binder particles. The microstructure rapidly evolved, with the evidence of the formation of a reaction phase (matrix) already after 230 s after water deposition, and indeed the reaction appears to have been driven by small particles of binders that were pushed out by the deposition of the water drops. In any case, we should be aware of the fact that the way we deposited the water drops for the *in situ* tomographic analysis is different from the actual process carried out during binder jetting by the printers, both in terms of the total volume of water, the number of locations where it was deposited and its impact velocity on the powder bed. Therefore, the results reported in this work are to be taken as mainly qualitative.

Similar heterogeneities were observed in the samples produced with the two printers: between layers of higher density, a region of matrix in which voids with a circular shape were present was observed, spaced by a distance compatible with the voxel size employed while printing. At a smaller scale, pores with a size of up to a millimeter were revealed by tomographic analyses, even in the areas with the highest density. Some of these pores are the result of the dissolution of MKP particles during printing, as observed by the *in situ* monitoring of the microstructural evolution of the powder bed after water deposition. In fact, pores of shape similar to the initial MKP particles can be observed in the microstructure (Figs. 11 and 12), similarly to what has also been highlighted during the monitoring of gypsum plaster setting with *in situ* X-ray tomographic experiments.

The difference in pore size and size distribution between samples produced with the two printers is, also, related to the use of smaller MKP particles in the case of the small printer. This could explain the observed difference in the maximum density, being 85–90 and 75% for the samples manufactured with the small and large printer, respectively. Indeed, a similar finding was obtained in the case of gypsum plaster, where it was observed that by using binder particles of different sizes it was possible to vary the size of the resulting pores [64].

Further work will focus on devising a way of more closely replicating the printer's water deposition process inside the tomograph, and to increase the contrast between the sand particles and the binder matrix, for instance using marble particles.

4. Conclusions

Large scale additive manufacturing by Binder Jetting of lightweight artificial stone components was possible by adding two reactive components (MgO and MKP) in particle form to a powder bed, generating a fast setting potassium magnesium phosphate phase (K-Struvite) upon contact with water. While the formation of the binder phase was confirmed by XRD analysis, demonstrating that even a fast process such as Binder Jetting enabled achieving the desired reaction, the presence of some unreacted MgO particles was observed.

Produced parts possessed a large amount (~40–50 vol%) of mainly open residual porosity, with compression strength depending on both the voxel size (type of printer) adopted and the composition of the powder bed (addition of lightweight glass particles or not).

XCT investigations on the dry powder bed enabled to assess the presence of artifacts due to the powder layer deposition, namely lower density regions at the interface between individual layers which were present also in the printed samples although to a much larger extent in this latter case. Analysis of the effect of water deposition on the powder bed showed that particle redistribution occurred, as well as (partial) dissolution of the soluble component (MKP) of the two-part reactive binder system. The impact of the water droplet in the *in situ* experiments generated cavities that could also be observed in the microstructure of the samples produced by the actual printers, homogeneously spaced according to the printer's voxel size.

The present study demonstrated that X-ray microtomography analysis permits to correlate significant microstructural features, such as the size and shape of pores and their location within the volume of samples, with the processing steps used for their manufacture.

Declaration of competing interest

The authors declare that they have no known competing financial interests or personal relationships that could have appeared to influence the work reported in this paper.

Acknowledgments

The work was carried out in the framework of the H2020-MSCA-

RISE-2016 “AMITIE” and the RIR-FESR 2017 “ADMIN4D” projects.

References

[1] Y. Huang, M.C. Leu, J. Mazumder, A. Donmez, Additive manufacturing: current state, future potential, gaps and needs, and recommendations, J. Manuf. Sci. Eng. Trans. 137 (2015) 1–10.

[2] B.P. Conner, et al., Making sense of 3-D printing: creating a map of additive manufacturing products and services, Addit. Manuf. 1–4 (2014) 64–76.

[3] A.M. Tofail, E.P. Koumoulos, A. Bandyopadhyay, S. Bose, L. O'Donoghue, C. Charitidis, Additive manufacturing: scientific and technological challenges, market uptake and opportunities, Mater. Today 21 (2018) 22–37.

[4] H. Paris, H. Mokhtarian, E. Coatanéa, M. Museau, I.F. Ituarte, Comparative environmental impacts of additive and subtractive manufacturing technologies, CIRP Ann 65 (2016) 29–32.

[5] C.W. Hull, Apparatus for Production of Three Dimensional Objects by Stereolithography, 1986, p. US4575330A.

[6] A. Zocca, P. Colombo, et al., Additive manufacturing of ceramics: issues, potentialities, and opportunities, J. Am. Ceram. Soc. 98 (2015) 1983–2001.

[7] X. Wei, Y. Liu, D. Zhao, S.S. Ge, 3D printing of piezoelectric barium titanate with high density from milled powders, J. Eur. Ceram. Soc. 40 (2020) 5423–5430.

[8] Y. Liu, et al., 3D printing of ceramic cellular structures for potential nuclear fusion application, Add. Manuf. 35 (2020) 101348.

[9] G. Ding, R. He, K. Zhang, N. Zhou, H. Xu, Stereolithography 3D printing of SiC ceramic with potential for lightweight optical mirror, Ceram. Int. 46 (2020) 18785–18790.

[10] A. Butscher, et al., New depowdering-friendly designs for three-dimensional printing of calcium phosphate bone substitutes, Acta Biomater. 9 (2013) 9149–9158.

[11] M.D.M. Innocentini, et al., Lattice-shaped geopolymer catalyst for biodiesel synthesis fabricated by additive manufacturing, Ceram. Int. 45 (2019) 1443–1446.

[12] F. Zhou, S. Han, Q. Qian, Y. Zhu, 3D printing of free-standing and flexible nitrogen doped graphene/polyaniline electrode for electrochemical energy storage, Chem. Phys. Lett. 728 (2019) 6–13.

[13] K. Huang, H. Elsayed, G. Franchin, P. Colombo, Complex SiOC ceramics from 2D structures by 3D printing and origami, Add. Manuf. 33 (2020) 101144.

[14] E. MacDonald, et al., Fabricating patch antennas within complex dielectric structures through multi-process 3D printing, J. Manuf. Process. 34 (2018) 197–203.

[15] R.A. Buswell, R.C. Soar, A.G.F. Gibb, A. Thorpe, Freeform construction: mega-scale rapid manufacturing for construction, Autom. ConStruct. 16 (2007) 224–231.

[16] G. De Schutter, K. Lesage, V. Mechtcherine, V.N. Nerella, G. Habert, I. Agusti-Juan, Vision of 3D printing with concrete- Technical, economic and environmental potentials, Cem, Concr. Res. 112 (2018) 25–36.

[17] B. Nematollahi, M. Xia, J. Sanjayan, Current progress of 3D concrete printing technologies, in: ISARC 2017- Proceedings of the 34th International Symposium on Automation and Robotics in Construction, Isarc, 2017, pp. 260–267.

[18] S. Lim, R.A. Buswell, T.T. Le, S.A. Austin, A.G.F. Gibb, T. Thorpe, Developments in construction-scale additive manufacturing processes, Autom. ConStruct. 21 (2012) 262–268.

[19] J.G. Sanjayan, B. Nematollahi, M. Xia, T. Marchment, Effect of surface moisture on inter-layer strength of 3D printed concrete, Construct. Build. Mater. 172 (2018) 468–475.

[20] V.N. Nerella, V. Mechtcherine, Studying the Printability of Fresh Concrete for Formwork-free Concrete Onsite 3D Printing Technology (CONPrint3D), 3D Concrete Printing Technology, 2019, pp. 333–347.

[21] B. Khoshnevis, S. Bukkapatnam, H. Kwon, J. Saito, Experimental investigation of contour crafting using ceramics materials, Rapid Prototyp. J. 7 (2001) 32–42.

[22] M. Krause, J. Otto, A. Bulgakov, D. Sayfeddine, Strategic optimization of 3D-concrete-printing using the method of CONPrint3D®, in: ISARC 2018- 35th International Symposium on Automation and Robotics in Construction and International AEC/FM Hackathon, The Future of Building Things, 2018 (Isarc).

[23] C. Gosselin, R. Duballet, P. Roux, N. Gaudillière, J. Dirrenberger, P. Morel, Large-scale 3D printing of ultra-high performance concrete - a new processing route for architects and builders, Mater. Des. 100 (2016) 102–109.

[24] A. Pierre, D. Weger, A. Perrot, D. Lowke, Penetration of cement pastes into sand packings during 3D printing: analytical and experimental study, Mater. Struct. Constr. 51 (2018) 1–12.

[25] G. Cesaretti, E. Dini, X. De Kestelier, V. Colla, L. Pambaguian, Building components for an outpost on the Lunar soil by means of a novel 3D printing technology, Acta Astronaut. 93 (2014) 430–450.

[26] G.J. Gibbons, R. Williams, P. Purnell, E. Farahi, 3D Printing of cement composites, Adv. Appl. Ceram. 109 (2010) 287–290.

[27] P. Shakor, J. Sanjayan, A. Nazari, S. Nejadi, Modified 3D printed powder to cement-based material and mechanical properties of cement scaffold used in 3D printing, Construct. Build. Mater. 138 (2017) 398–409.

[28] E. Vorndran, et al., Hydraulic setting $Mg_3(PO_4)_2$ powders for 3D printing technology, Adv. Appl. Ceram. 110 (2011) 476–481.

[29] M. Xia, B. Nematollahi, J. Sanjayan, Printability, accuracy and strength of geopolymer made using powder-based 3D printing for construction applications, Autom. ConStruct. 101 (2019) 179–189.

[30] I. Buj, J. Torras, M. Rovira, J. de Pablo, Leaching behaviour of magnesium phosphate cements containing high quantities of heavy metals, J. Hazard Mater. 175 (2010) 789–794.

[31] E. Vorndran, et al., Hydraulic setting $Mg_3(PO_4)_2$ powders for 3D printing technology, Adv. Appl. Ceram. 110 (2011) 476–481.

[32] U. Klammert, E. Vorndran, T. Reuther, F.A. Müller, K. Zorn, U. Gbureck, Low temperature fabrication of magnesium phosphate cement scaffolds by 3D powder printing, J. Mater. Sci. Mater. Med. 21 (2010) 2947–2953.

[33] E. Vorndran, et al., Hydraulic setting $Mg_3(PO_4)_2$ powders for 3D printing technology, Adv. Appl. Ceram. 110 (2011) 476–481.

[34] M. Le Rouzic, T. Chaussadent, L. Stefan, M. Saillio, On the influence of Mg/P ratio on the properties and durability of magnesium potassium phosphate cement pastes, Cement Concr. Res. 96 (2017) 27–41.

[35] B. Xu, H. Ma, Z. Li, Influence of magnesia-to-phosphate molar ratio on microstructures, mechanical properties and thermal conductivity of magnesium potassium phosphate cement paste with large water-to-solid ratio, Cement Concr. Res. 68 (2015) 1–9.

[36] P.J. Withers, C. Bouman, et al., X-ray computed tomography, Nature Reviews Methods Primers 1 (2021) 18.

[37] E. Maire, P.J. Withers, Quantitative X-ray tomography, Int. Mater. Rev. 59 (2014) 1–43.

[38] V. Mazars, O. Caty, et al., Damage investigation and modeling of 3D woven ceramic matrix composites from X-ray tomography in-situ tensile tests, Acta Mater. 140 (2017) 130–139.

[39] L. Saucedo-Mora, P.T. Lowe, et al., In situ observation of mechanical damage within a SiC-SiC ceramic matrix composite, J. Nucl. Mater. 481 (2016) 13–23.

[40] S.C. Wu, T.Q. Xiao, et al., The imaging of failure in structural materials by synchrotron radiation X-ray microtomography, Eng. Fract. Mech. 182 (2017) 127–156.

[41] C.L.A. Leung, S. Marussi, et al., In situ X-ray imaging of defect and molten pool dynamics in laser additive manufacturing, Nat. Commun. 9 (2018) 1–9.

[42] P. Lhuissier, X. Bataillon, et al., In situ 3D X-ray microtomography of laser-based powder-bed fusion (L-PBF)-A feasibility study, Add. Manuf. (2020) 101271.

[43] N.D. Parab, J.E. Barnes, et al., Real time observation of binder jetting printing process using high-speed X-ray imaging, Sci. Rep. 9 (2019) 1–10.

[44] J.M. Hundley, Z.C. Eckel, et al., Geometric characterization of additively manufactured polymer derived ceramics, Add. Manuf. 18 (2017) 95–102.

[45] A. Thompson, I. Maskery, et al., X-ray computed tomography for additive manufacturing: a review, Meas. Sci. Technol. 27 (2016), 072001.

[46] I. Maskery, N.T. Aboulkhair, et al., Quantification and characterisation of porosity in selectively laser melted Al–Si10–Mg using X-ray computed tomography, Mater. Char. 111 (2016) 193–204.

[47] S. Diener, G. Franchin, et al., X-ray microtomography investigations on the residual pore structure in silicon nitride bars manufactured by direct ink writing using different printing patterns, Op. Ceram. 5 (2021) 100042.

[48] J.Y. Buffiere, E. Maire, et al., In situ experiments with X ray tomography: an attractive tool for experimental mechanics, Exp. Mech. 50 (2010) 289–305.

[49] J. Schindelin, I. Arganda-Carreras, et al., Fiji: an open-source platform for biological-image analysis, Nat. Methods 9 (2012) 676–682.

[50] M. Abramoff, P. Magalhaes, et al., Image processing with ImageJ, J. Biophotonics Int. 11 (2004) 36–42.

[51] R. Dougherty, K. Kunzelmann, Computing local thickness of 3D structures with ImageJ, Microsc. Microanal. 13 (2007) 1678–1679.

[52] M. Arlete Carvalho, A.M. Segadães, The hydration of magnesium phosphate cements: effect of powder characteristics on the reaction kinetics, Mater. Sci. Forum 591–593 (2008) 833–838.

[53] J.W. Park, K.H. Kim, K.Y. Ann, Fundamental properties of magnesium phosphate cement mortar for rapid repair of concrete, Ann. Mater. Sci. Eng. (2016) 1–7.

[54] H. Ma, B. Xu, Potential to design magnesium potassium phosphate cement paste based on an optimal magnesia-to-phosphate ratio, Mater. Des. 118 (2017) 81–88.

[55] E. Soudée, J. Péra, Mechanism of setting reaction in magnesia-phosphate cements, Cement Concr. Res. 30 (2000) 315–321.

[56] A.S. Wagh, S.Y. Jeong, Chemically bonded phosphate ceramics: I, A dissolution model of formation, J. Am. Ceram. Soc. 86 (2003) 1838–1844.

[57] M. Le Rouzic, T. Chaussadent, G. Platret, L. Stefan, Mechanisms of k-struvite formation in magnesium phosphate cements, Cement Concr. Res. 91 (2017) 117–122.

[58] B. Xu, B. Lothenbach, A. Leemann, F. Winnefeld, Reaction mechanism of magnesium potassium phosphate cement with high magnesium-to-phosphate ratio, Cement Concr. Res. 108 (2018) 140–151.

[59] X. Chen, S. Wu, J. Zhou, Influence of porosity on compressive and tensile strength of cement mortar, Construct. Build. Mater. 40 (2013) 869–874.

[60] A. López-Uceda, J. Ayuso, M. López, J. Jimenez, F. Agrela, M. Sierra, Properties of non-structural concrete made with mixed recycled aggregates and low cement content, Materials 9 (2016) 74.

[61] Y. Koubaa, M. Jamei, H. Guiras, Hydro-mechanical properties of highly porous limestone rock used for historic monuments in north-East Tunisia, J. Civ. Environ. Eng. 8 (2018) 3.

[62] S. Yüksek, Mechanical properties of some building stones from volcanic deposits of mount Erciyes (Turkey), Materialesde ConstruCCión. 69 (2019) 187.

[63] V. Festa, A. Fiore, M. Luisi, M.N. Miccoli, L. Spalluto, Petrographic features influencing basic geotechnical parameters of carbonate soft rocks from Apulia (southern Italy), Eng. Geol. 233 (2018) 76–97.

[64] J. Adrien, S. Meille, S. Tadier, E. Maire, L. Sasaki, In-situ X-ray tomographic monitoring of gypsum plaster setting, Cement Concr. Res. 82 (2016) 107–116.

[65] N. Lardier, P. Roudier, et al., High speed photography of water drop impacts on sand and soil, Eur. J. Soil Sci. 70–2 (2019) 245–256.